JOURNAL OF MAGNETIC RESONANCE **134,** 171–175 (1998)
ARTICLE NO. MN981521

Chemical Shift Imaging in Rotating Solids by Radiofrequency Field Gradients

C. Malveau, B. Diter, P. Tekely, and D. Canet[1]

Laboratoire de Méthodologie RMN,[2] Université H. Poincaré, BP 239, 54506 Vandoeuvre-les-Nancy Cedex, France

Received November 25, 1997; revised March 20, 1998

A dedicated equipment has been designed for solid state NMR imaging in the spatial direction coinciding with the rotation axis of a ^{13}C CP/MAS probe. It involves a two-turn B_1 gradient coil whose plane is perpendicular to that axis and a ^{1}H–^{13}C doubly tuned saddle coil used for normal spectroscopic operations, orthogonal to the latter. The experiment provides a two-dimensional diagram with ^{13}C chemical shift in one dimension whereas the second dimension corresponds to the space variable. Some test experiments demonstrate the validity of this approach.

Key Words: **CP/MAS NMR; chemical shift imaging; radiofrequency field gradient; NMR probe; 2D experiment.**

NMR imaging methods in the solid state are hampered by the importance of linewidths which thus require huge gradients and/or line narrowing procedures (*1–3*). This is especially true for proton NMR imaging. Indeed, because proton offers the best sensitivity, a large variety of experiments have been proposed in this respect (*4–21*), leading, most of the time, only to spin density images, i.e., devoid of chemical shift information. An alternative approach for circumventing the linewidth problem is to turn to high resolution spectroscopy of rare spins (*22–25*) with cross-polarization and under magic angle spinning and dipolar decoupling (*26–28*). In addition, compared to proton imaging, this may provide a much better discrimination of the different species through their chemical shifts. It is actually this type of experiment which is addressed in the present paper. Except problems associated with the low sensitivity of such nuclei (for example, ^{13}C at natural abundance), difficulties arise from (1) the synchronization of the gradient with sample rotation if it is applied perpendicularly to the rotation axis and (2) the spreading of resonance frequencies if B_0 gradients are used; this spreading may entail off-resonance effects which alter the Hartmann–Hahn condition and the efficiency of dipolar decoupling (*29*). Moreover, such experiments run with B_0 gradients are rather instrumentally demanding. Nevertheless, examples of spin density images are relatively frequent and even separate images of chemically shifted species could be obtained, for instance, by selecting a characteristic peak of a given compound (*25*).

It is in fact our objective to perform a so-called two-dimensional chemical-shift imaging experiment, with one dimension associated with chemical shift, the second one corresponding to a spatial variable. Aiming at instrumental simplicity, we have chosen the direction of the spinning axis as the examined spatial dimension (this avoids the use of synchronized oscillating gradient (*26–28*)) and a B_1 gradient rather than a B_0 gradient. It proved possible (*30*) to create a B_0 gradient along the spinning axis, however, by means of the combination of two gradients acting along perpendicular directions. This latter choice is dictated by several advantages of B_1 gradients over B_0 gradients: (1) they are immune to magnetic susceptibility variations across the sample, contrary to B_0 gradient systems, which would suffer from internal gradients due to possible magnetic susceptibility changes along the spinning axis direction (in other directions, it is likely that sample spinning would remove the effect of these internal gradients); (2) they afford negligible raise and fall times; (3) they do not produce any additional shift, thus eliminating the need of special decoupling procedures; (4) it is relatively easy to create a B_1 gradient along the spinning axis direction; (5) for a long time, chemical-shift imaging techniques with B_1 gradients have proven to be quite reliable (*31*).

We begin with a brief description of the probe which has already been discussed in the context of self-diffusion measurements (*32*). The gradient coil, tuned at the carbon-13 frequency, is located in a plane perpendicular to the spinning axis whereas the coil devoted to pure spectroscopic operations must be of the saddle type (Fig. 1, from Ref. (*32*)) so as to fulfill the requirement of orthogonality between the two coils. The gradient coil, comprising two turns of diameter 22 and 18 mm, respectively, delivers a B_1 gradient of 21 G/cm for a RF power of 300 W. Other coil geometries could be considered in order to improve the performance of this experimental setup. The saddle coil has the following dimensions: height of 8.2 mm and diameter of 8 mm. Moreover, it must be doubly tuned for proton and carbon-13 (in the present case) with appropriate stop-circuits on both channels. Pulse lengths are carbon-13 90° pulse: 8.5 μs for a RF power of 200 W; proton 90° pulse: 8.2 μs for a RF power of 40 W. For both coils, high voltage capacitors were used in order to deal possibly with large RF

[1] To whom correspondence should be addressed.
[2] UPRESA CNRS 7042, FU CNRS 1742 (INCM).

1090-7807/98 $25.00

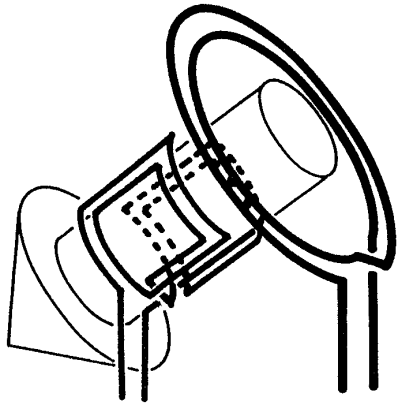

FIG. 1. A sketch of the coil assembly used for performing the ^{13}C chemical-shift imaging experiment in rotating solids (from Ref. (*32*)).

power. Leakage between the two coils is rather critical; it is optimized by gently adjusting the position of the connection wires (an isolation factor of 35 dB being currently achieved). Finally, the orientation and position of the coil assembly with respect to the sample (Andrew type rotor) can be finely modified by a mechanical device. Experiments were run on a homemade spectrometer equipped with a 4.7-T wide-bore vertical magnet. Three amplifiers are necessary: a Kalmus 163 HP amplifier operating at 200 MHz for cross polarization and dipolar decoupling, a Bruker B-LAX 1000 operating at 50 MHz and used at the cross polarization stage, a Bruker B-LAX 300 RS operating at 50 MHz for feeding the gradient coil.

The chemical-shift imaging pulse sequence is relatively simple and is schematized in Fig. 2. The phase cycling serves merely to eliminate artifacts and the sequence will be discussed according to the first phase cycle step. It starts classically by polarization transfer from proton to carbon-13. At this stage, carbon magnetization is along the x axis of the rotating frame. Spatial encoding stems from the application of a B_1 gradient pulse along the y axis of the rotating frame. It can be recalled that the relative phases of the two carbon-13 transmitters must be adjusted so that they act in the same rotating frame (*33*). The B_1 gradient pulse produces a nutation in the xz plane which results in an amplitude modulation for the x component of magnetization,

$$S(t_1) = \rho(X)\cos(2\pi kX) \qquad [1]$$

with the usual k variable, $k = \gamma g_1 t_1/2\pi$ (g_1, gradient amplitude), X being the spatial variable associated with the direction of the spinning axis, and $\rho(X)$ the relevant spin density. The acquired signal, obtained under dipolar decoupling, is thus of the form

$$S(t_1, t_2) = \sum_j \rho(X, \nu_j)\cos(2\pi kX)\exp(2i\pi\nu_j t_2), \qquad [2]$$

where ν_j is the resonance frequency of the jth peak in the conventional spectrum (in [1] and [2] relaxation effects have been omitted). A double Fourier transform of [2] will therefore yield for each resonance the spin density as a function of the space variable X. It can be mentioned that the Fourier transform with respect to k is a real one which leads to pure absorption peaks and avoids consequently any phase twist effect. It must also be mentioned that, by contrast with B_0 gradients, it is recommended to increment the gradient pulse duration rather than the gradient amplitude. This is to prevent off-resonance effects which are prone to occur due to the large carbon-13 spectral widths. As a consequence, a damping factor of the form $\exp(-t_1/T_{1,2}) = \exp(-2\pi k/\gamma g_1 T_{1,2})$ must be included in Eq. [1]; $T_{1,2}$ is the effective relaxation time of nutating magnetization and is such that $1/T_{1,2} = (1/2)(1/T_1 + 1/T_2)$ (*34*). This leads to the "theoretical" spatial resolution

$$\Delta X = \frac{1}{\gamma g_1}\left(\frac{1}{T_1} + \frac{1}{T_2}\right) \approx \frac{1}{\gamma g_1 T_2} \qquad [3]$$

since in solids T_2 is usually much shorter than T_1. For instance, this would yield, with a gradient of 21 G/cm, a spatial resolution of 0.1 μm for adamantane (natural T_2 of 635 ms). This value is obviously unrealistic because it does not account for all factors which reduce the actual spatial resolution (*3*) and because adamantane has an exceptionally long T_2. Nevertheless, this figure illustrates the potentiality of the method which is not affected by magnetic susceptibility variations across the sample (and consequently by B_0 gradients which appear at interfaces in a heterogeneous

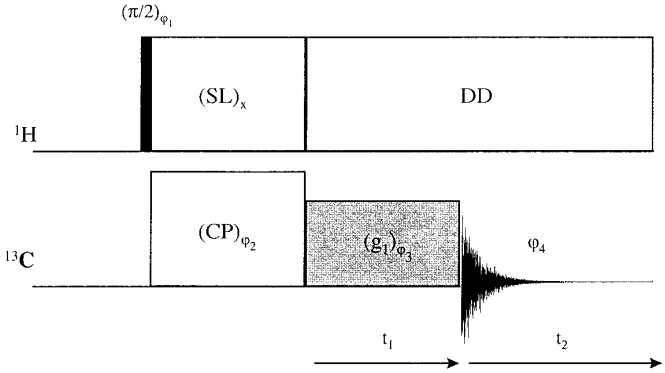

FIG. 2. The chemical-shift imaging pulse sequence. After the cross polarization stage, a B_1 gradient pulse, applied during t_1, generates spatial encoding. The signal is thereafter normally acquired during t_2. The phase cycling is

φ_1	φ_2	φ_3	φ_4
$+y$	$+x$	$+y$	$+x$
$-y$	$+x$	$+y$	$-x$
$+y$	$+x$	$-y$	$+x$
$-y$	$+x$	$-y$	$-x$

and can be appended by a CYCLOPS procedure (φ_2, φ_3, and φ_4).

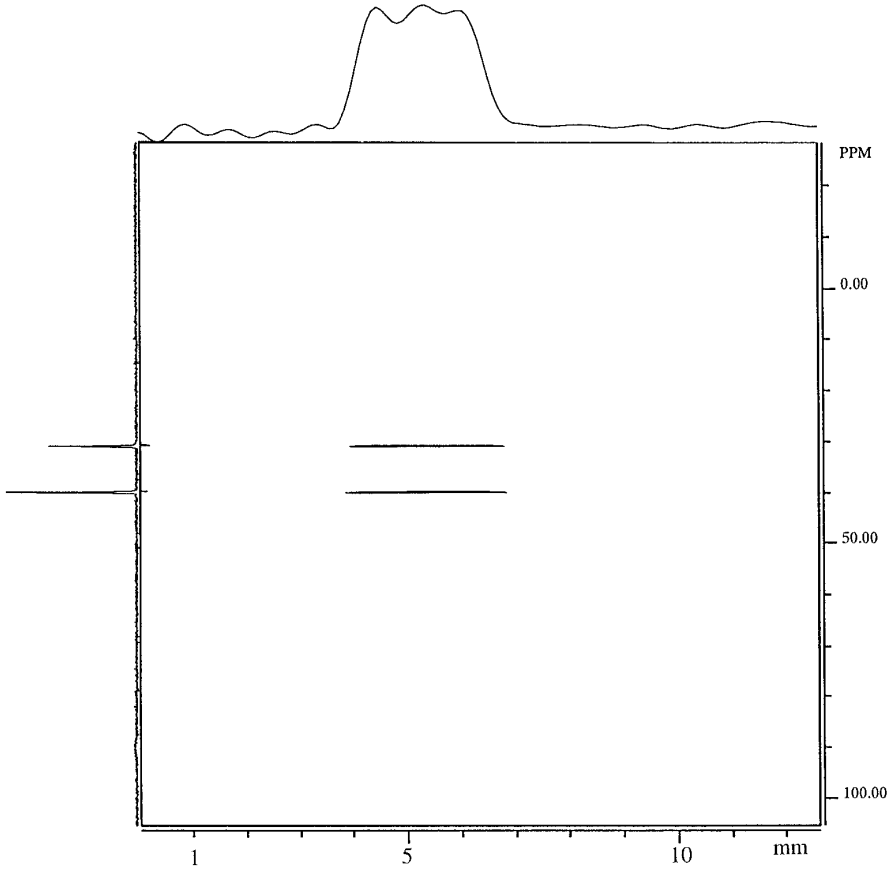

FIG. 3. The experiment of Fig. 2 applied to a rotating (2.5 kHz) sample of adamantane (4 mm i.d., 3 mm in height along the imaging axis). Cross-polarization time, 7 ms; 32 t_1 values incremented by 14 μs (zero-filled to 256 points); 4K data points in the t_2 dimension (zero-filled to 8K), 128 scans for each t_1 increment; recycle time, 5 s.

sample). Indeed, Eq. [3] reminds one that the spatial resolution is governed by the natural T_2 and not by T_2^* as it may be the case with B_0 gradient experiments.

Once the experiment itself has proven to be feasible (a typical "fast" experiment performed with an adamantane sample requires a measuring time of about 40 minutes), the next step is to determine a region where the gradient is uniform. This has been achieved by positioning in a trial and error fashion the rotor whose cylinder (4 mm i.d.) is filled with 2 mm in height of adamantane powder. The result is that the gradient is uniform in a region corresponding at least to a cylinder of 4-mm diameter and of 3.5-mm height. It can also be mentioned that this diameter is sufficiently small so that the B_1 field is constant within a given plane perpendicular to the spinning axis, reducing to negligible level any gradient shift. Further assessment of the gradient uniformity is provided by the images themselves. Figure 3 shows the 2D spectrum of a 4-mm-i.d. sample containing 3 mm in height of adamantane powder. This spectrum is especially clean, the only visible artifacts being two tiny axial peaks and some slight spurious oscillations at the top of the profile. Indeed, the same length is observed for the two traces and the profile (projection along the chemical-shift axis) exhibits the expected shape with sharp edges. The next sample that we have investigated contains adamantane in the lower compartment and hexamethylbenzene (HMB) in the upper compartment; both compartments have roughly the same height (ca. 1.5 mm). The separator (thickness, 470 μm) is made of teflon. The image, shown in Fig. 4, has been limited to the aliphatic carbons (CH_3 of HMB; CH and CH_2 of adamantane). In addition to comments similar to those given for Fig. 3, we can mention that the separator is clearly visible and can be accurately located. The remaining slight distorsions in the profiles (obtained by projection along the chemical-shift dimension) are believed to arise from a relatively poor sensitivity and/or to a non-uniform receptivity of the saddle coil.

The above examples demonstrate the feasibility of ^{13}C chemical-shift imaging in rotating solids by B_1 gradients with, potentially, an excellent spatial resolution. The use of the technique for real world problems should however await some technical improvements especially at the saddle coil level, which should accept more important RF power and whose sensitivity might be increased. Also, the dimensions of both the gradient coil and the saddle coil could be reconsidered in view of examining larger samples.

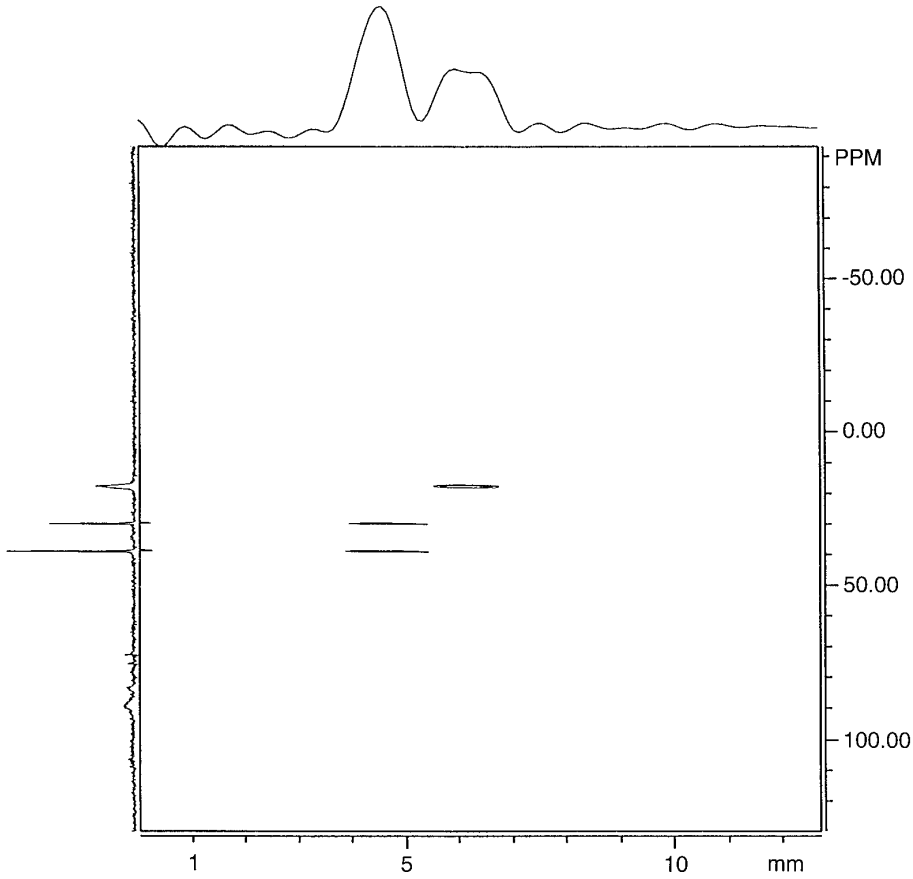

FIG. 4. Same experiment as in Fig. 3 with a sample made of two compartments, one filled with adamantane powder, the other with HMB powder; 256 scans for each t_1 increment.

REFERENCES

1. P. Blümer and B. Blümich, NMR imaging of solids, *in* "NMR 30 Solid-State NMR. I. Methods," pp. 209–277 (1994).
2. J. B. Miller, D. G. Cory, and A. N. Garroway, Line-narrowing approaches to solid-state NMR imaging: Pulsed gradients and second averaging, *Philos. Trans. R. Soc. London A* **333,** 413–426 (1990).
3. P. T. Callaghan, "Principles of Nuclear Magnetic Resonance Microscopy," Oxford Univ. Press, Oxford (1995).
4. A. A. Samoilenko, D. Yu. Artemov, and L. A. Sibeldina, Formation of sensitive layer in experiments on NMR subsurface imaging, *JETP Lett.* **47,** 417–419 (1988).
5. S. Emid and J. H. N. Creyghton, High resolution NMR imaging in solids, *Phys. B* **128,** 81–83 (1985).
6. E. Rommel, S. Hafner, and R. Kimmich, NMR imaging of solids by Jeener–Broekart phase encoding, *J. Magn. Reson.* **86,** 264–272 (1990).
7. D. G. Cory and W. S. Veeman, Applications of line narrowing to ^{1}H NMR imaging of solids, *J. Magn. Reson.* **84,** 392–397 (1989).
8. S. Matsui, A. Uraoka, and T. Inouye, Improved resolution in solid-state NMR imaging by self-phase encoding, *J. Magn. Reson. A* **112,** 130–133 (1995).
9. S. Matsui, A. Uraoka, and T. Inouye, Solid-state NMR imaging by tetrahedral-magic-echo time-suspension sequences, *J. Magn. Reson. A* **120,** 11–17 (1996).
10. P. J. Mc Donald, J. J. Attard, and D. G. Taylor, A new approach to the NMR imaging of solids, *J. Magn. Reson.* **72,** 224–229 (1987).
11. S. Matsui, Y. Ogasawara, and T. Inouye, Proton images of elastomers by solid-state NMR imaging, *J. Magn. Reson. A* **105,** 215–218 (1993).
12. D. E. Demco, S. Hafner, and R. Kimmich, Spatially resolved homonuclear solid-state NMR. III. Magic-echo and rotary-echo phase-encoding imaging, *J. Magn. Reson.* **96,** 307–322 (1992).
13. F. De Luca, B. C. De Simone, N. Lugeri, B. Maraviglia, and C. Nuccetelli, Rotating-frame spin-echo imaging in solids, *J. Magn. Reson.* **90,** 124–130 (1990).
14. F. Weigand, B. Blümich, and H. W. Spiess, Application of nuclear magnetic resonance magic sandwich echo imaging to solid polymer, *Solid State NMR* **3,** 59–66 (1994).
15. W. S. Veeman and D. G. Cory, ^{1}H Nuclear magnetic resonance imaging of solids with magic-angle spinning, *Adv. Magn. Reson.* **13,** 43–56 (1989).
16. M. Buszko and G. E. Maciel, Magnetic-field-gradient-coil system for solid-state MAS and CRAMPS NMR imaging, *J. Magn. Reson. A* **107,** 151–157 (1994).
17. D. G. Cory, A. M. Reichwein, J. W. M. Van Os, and W. S. Veeman, NMR images of rigid solids, *Chem. Phys. Lett.* **143,** 467–470 (1988).
18. A. N. Garroway, J. Baum, M. G. Munowitz, and A. Pines, NMR imaging in solids by multiple-quanta resonance, *J. Magn. Reson.* **60,** 337–341 (1984).

19. J. B. Miller, D. G. Cory, and A. N. Garroway, Pulsed field gradient NMR imaging of solids, *Chem. Phys. Lett.* **164,** 1–4 (1989).

20. S. L. Dieckman, P. Rizo, N. Gopalsani, J. P. Heeschen, and R. E. Botto, Three-dimensional microscopic ^{1}H NMR imaging of rigid polymers, *J. Am. Chem. Soc.* **114,** 2717–2719 (1992).

21. H. M. Cho, C. J. Lee, D. N. Skykind, and D. P. Weitekamp, Nutation sequences for magnetic resonance imaging in solids, *Phys. Rev. Lett.* **55,** 1923–1926 (1985).

22. N. M. Szeverenyi and G. E. Maciel, NMR spin imaging of magnetically dilute nuclei in the solid state, *J. Magn. Reson.* **60,** 460–466 (1984).

23. J. B. Miller and A. N. Garroway, Carbon-13 refocused gradient imaging of solids, *J. Magn. Reson.* **85,** 255–264 (1989).

24. E. Günther, B. Blümich, and H. W. Spiess, Molecular order and density of skin and core in drawn polypropylene investigated by spectroscopic ^{13}C NMR imaging, *Macromolecules* **25,** 3315–3316 (1992).

25. M. F. Davies and G. E. Maciel, Rare-spin solid-state NMR imaging using chemical-shift-selective excitation, *J. Magn. Reson.* **94,** 617–624 (1991).

26. U. Scheler, J. J. Titman, B. Blümich, and H. W. Spiess, Spatially resolved two-dimensional solid-state NMR spectroscopy, *J. Magn. Reson. A* **107,** 251–254 (1994).

27. D. G. Cory and W. S. Veeman, ^{13}C Imaging of solids with magic angle sample spinning, *J. Phys. E* **22,** 180–184 (1989).

28. U. Scheler, B. Blümich, and H. W. Spiess, Spinning sidebands from chemical shift anisotropy in ^{13}C MAS imaging, *Solid State NMR* **2,** 105–110 (1993).

29. Y. Sun, J. Xiong, H. Lock, M. L. Buszko, J. A. Haase, and G. E. Maciel, Solid-state ^{13}C NMR imaging with magic-angle spinning, *J. Magn. Reson. A* **110,** 1–6 (1994).

30. W. E. Maas, F. H. Laukien, and D. G. Cory, Gradient, high resolution, magic angle sample spinning NMR, *J. Am. Chem. Soc.* **118,** 13,085–13,086 (1996).

31. A. Haase, C. Malloy, and G. K. Radda, Spatial localization of high resolution ^{31}P spectra with a surface coil, *J. Magn. Reson.* **55,** 164–169 (1983).

32. C. Malveau, B. Diter, F. Humbert, and D. Canet, Self-diffusion measurements by carbon-13 NMR using radiofrequency field gradients, *J. Magn. Reson.* **130,** 131–134 (1998).

33. P. Maffei, P. Mutzenhardt, A. Retournard, B. Diter, R. Raulet, J. Brondeau, and D. Canet, NMR microscopy by radiofrequency field gradients, *J. Magn. Reson. A* **107,** 40–49 (1994).

34. H. C. Torrey, Transient nutations in nuclear magnetic resonance, *Phys. Rev.* **76,** 1059–1068 (1949).